

Quasi-Periodic Nanoripples in Graphene Grown by Chemical Vapor Deposition and Its Impact on Charge Transport

Guang-Xin Ni,^{†,‡,§,◆} Yi Zheng,^{†,‡,◆} Sukang Bae,^{†,◆} Hye Ri Kim,[†] Alexandre Pachoud,^{†,#} Young Soo Kim,^{†,▲} Chang-Ling Tan,[†] Danho Im,^{||} Jong-Hyun Ahn,^{†,¶} Byung Hee Hong,^{†,‡,*} and Barbaros Özyilmaz^{†,‡,§,#,*}

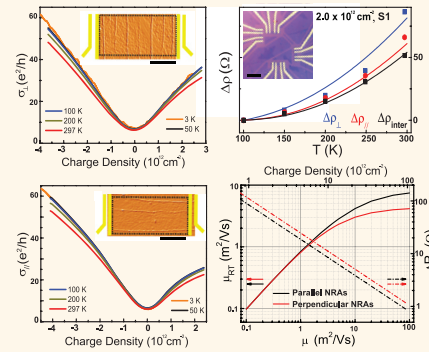
[†]Department of Physics, 2 Science Drive 3, National University of Singapore, Singapore 117542, [‡]NanoCore, 4 Engineering Drive 3, National University of Singapore, Singapore 117576, [§]Graphene Research Center, National University of Singapore, Singapore 117542, [¶]SKKU Advanced Institute of Nanotechnology (SAINT) and Center for Human Interface Nano Technology (HINT), ^{||}Department of Chemistry, and [#]School of Advanced Materials Science and Engineering, Sungkyunkwan University, Suwon 440-746, Korea, ^{*}NUS Graduate School for Integrative Sciences and Engineering (NGS), National University of Singapore, Singapore 117456, and [▲]Department of Chemistry and [▲]Department of Physics, Seoul National University, Seoul 151-747, Korea. [◆]These authors contributed equally to this work.

Graphene¹ is a promising material for many novel device applications such as ultrafast nanoelectronics, optoelectronics, and flexible transparent electronics.^{2–5} Cu-based CVD methods have now made wafer-scale graphene synthesis and transfer feasible both for single-layer graphene^{6,7} (SLG) and bilayer graphene (BLG).⁸ This not only brings the commercial applications of graphene within reach but also provides great advantages in introducing new substrates to enhance and engineer its electronic properties by tuning the substrate-induced screening^{9–12} and substrate-induced strain.^{13,14} Unlike CVD graphene growth on Ni,^{15,16} Cu-CVD graphene growth has a rather weak interaction with the underlying Cu substrate, allowing CVD graphene to grow continuously crossing atomically flat terraces, step edges, and vertices without introducing significant defects.¹⁷ Thus, by controlling pregrowth annealing⁷ and fine-tuning growth parameters,^{18,19} it is now possible to synthesize CVD graphene with submillimeter grain size. However, pregrowth annealing and CVD growth typically require high temperatures very close to the melting point of Cu at 1083 °C. This leads to Cu surface reconstruction and local surface melting^{17,20} during graphene growth, making high density Cu single-crystal terraces and step edges ubiquitous surface features. Taking into account the negative thermal expansion coefficient of graphene, this leads to new surface corrugations in CVD graphene during the cool down process.²¹ Previously, grain boundaries have been identified as one of the limiting factors to degrade

ABSTRACT The technical breakthrough in synthesizing graphene by chemical vapor deposition methods (CVD) has opened up enormous opportunities for large-scale device applications. To improve the electrical properties of CVD graphene grown on copper (Cu-CVD graphene), recent efforts have focused on increasing the grain size of such polycrystalline graphene films to 100 μm and larger. While an increase in grain size and, hence, a decrease of grain boundary density is expected to greatly enhance the device performance, here we show that the charge mobility and sheet resistance of Cu-CVD graphene is already limited within a single grain. We find that the current high-temperature growth and wet transfer methods of CVD graphene result in quasi-periodic nanoripple arrays (NRAs). Electron-flexural phonon scattering in such partially suspended graphene devices introduces anisotropic charge transport and sets limits to both the highest possible charge mobility and lowest possible sheet resistance values. Our findings provide guidance for further improving the CVD graphene growth and transfer process.

KEYWORDS: CVD graphene · quasi-periodic nanoripple arrays · anisotropic · charge transport · flexural phonon scattering · transparent electrodes · sheet resistance

graphene quality.²² While the heptagon and pentagon network^{22,23} at grain boundaries does disrupt the sp^2 delocalization of π electrons in graphene, it remains to be seen whether this is indeed the charge scattering source most relevant for device applications. In this paper, we show that Cu single-crystal step edges lead to the formation of quasi-periodic nanoripple arrays (NRAs) after transfer on Si/SiO₂ substrates. Such surface



* Address correspondence to
barbaros@nus.edu.sg,
byunghee@snu.ac.kr.

Received for review October 3, 2011
and accepted January 17, 2012.

Published online January 17, 2012
10.1021/nn203775x

© 2012 American Chemical Society

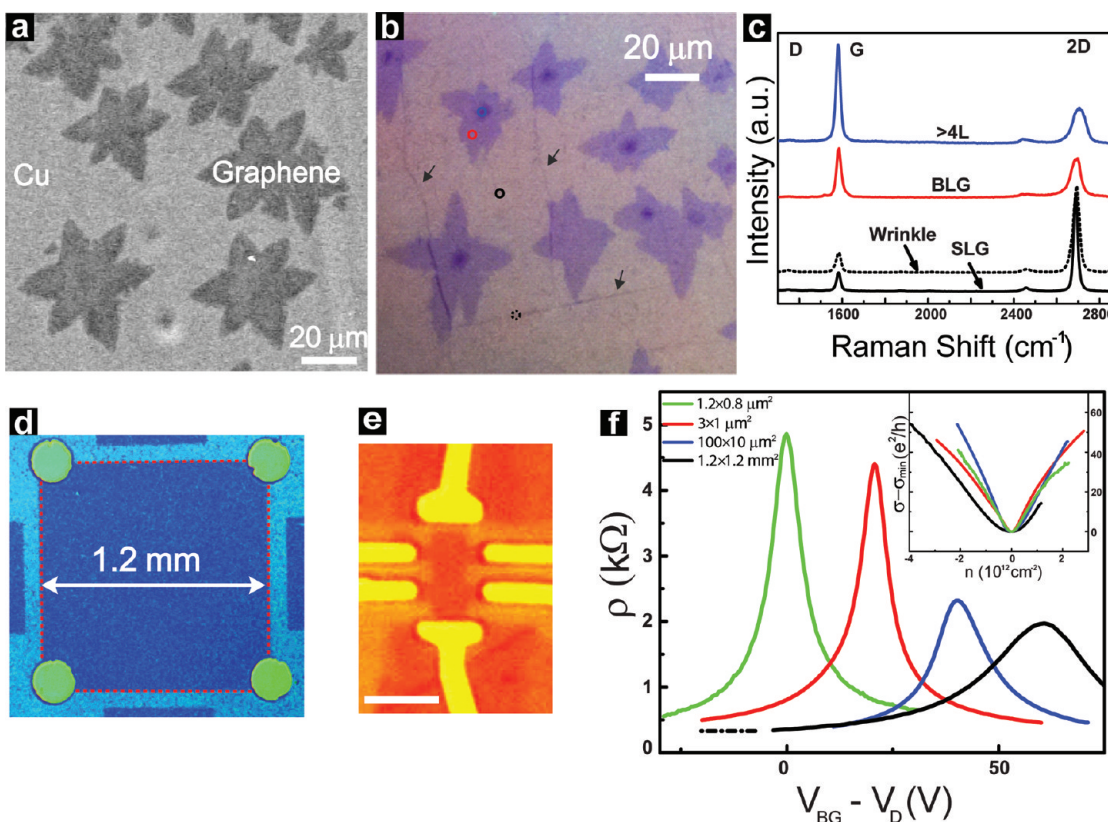


Figure 1. (a) SEM image of submonolayer graphene on Cu foil. (b) Optical image of high BL coverage CVD graphene on 300 nm SiO₂. The black, red, and blue circles indicate the Raman measurement (0.4 μm in spot size) locations. Black arrows indicate wrinkles formed during growth. (c) Raman spectroscopy of SLG, BLG, and multilayer graphene. Raman on optical visible wrinkle shows significant broadening in G and 2D peaks, indicating non-negligible strain. (d) Optical image of a millimeter size GFET with van der Pauw geometry and (e) of micrometer size. Scale bar: 2 μm . (f) Electrical measurements of square millimeter and square micrometer devices at RT. Each curve is shifted by +20 V. Inset show the corresponding $\sigma - \sigma_{\min}$ vs n .

corrugations suspend up to 20% of graphene and give rise to flexural phonon scattering. In particular, at room temperature and density levels of the order of $10^{12}/\text{cm}^2$, this leads to a strong anisotropy in the room temperature (RT) conductivity depending on the relative orientation between NRAs and current flow direction. More importantly, flexural phonon scattering within the nanoripples sets a lower bound on the sheet resistance and upper bound on the charge carrier mobility even in the absence of grain boundaries.

RESULTS AND DISCUSSION

We first compare the RT resistivity *versus* gate voltage (ρ vs V_{BG}) characteristics in four graphene field-effect transistors (GFETs) of very different dimensions, ranging from the micrometer scale to the millimeter scale. The resistivities of these devices, fabricated from the same batch of CVD graphene, are presented in Figure 1f. Surprisingly, except introducing stronger charge inhomogeneity, increasing the device channel area by 6 orders of magnitude does not significantly alter the charge carrier mobility; RT mobilities vary generally speaking independent of samples size for $\mu \sim 4000\text{--}6000 \text{ cm}^2/(\text{V}\cdot\text{s})$. This excludes grain boundaries (10–20 per mm; see Figure 1a) as the main limiting factor

for μ in our CVD graphene and strongly suggests that the main scatterers are identical to the ones in exfoliated graphene: adatoms and/or charged impurities. Similar conclusions have recently been reached also by ref 12.

However, high-resolution contact mode atomic force microscopy (AFM) of CVD graphene on Si/SiO₂ with ultrasharp tips reveals a new type of surface corrugations (Figure 2), whose influence on charge transport is not known. Distinct from the well-known low-density strain-induced wrinkles (~ 1 per $5 \mu\text{m}$), we observe nanoripples of $\sim 3 \pm 1 \text{ nm}$ in height of much higher density (~ 10 per $5 \mu\text{m}$), which are typically arranged in a quasi-periodic fashion (Figure 2b). Each nanoripple location contains multiple peaks of 10–20 nm width (see Figure 2e and Supporting Information), thus making it possible that overall a section of up to $\sim 100 \text{ nm}$, that is, up to 20% of the graphene sheet, becomes effectively suspended.

Systematic AFM studies on centimeter size samples further confirm that quasi-periodic nanoripple arrays (NRAs) are a general feature of the CVD graphene-on-SiO₂ surface morphology (see Supporting Information). To find out the origin of these NRAs, we carefully examined the single-crystal surface of Cu substrates. As shown in Figure 2a, thermally annealed Cu has a characteristically high density of single-crystal terraces and

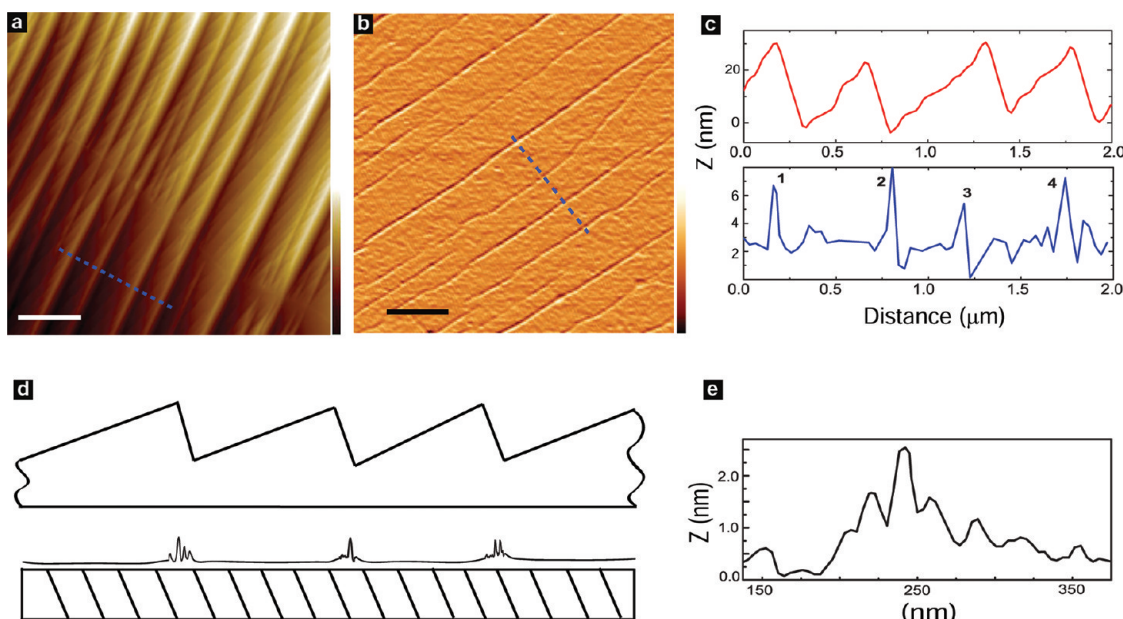


Figure 2. (a) AFM image of Cu surface, showing single-crystal terraces and step edges (color scale, 0–60 nm; scale bar = 1 μm), and (b) CVD graphene on SiO₂, showing high-density nanoripples induced by Cu step edges (color scale, 0–15 nm; scale bar = 1 μm). (c) Top: AFM cross section of Cu terraces. The typical width of step edges is ~ 100 nm. Bottom: AFM line scans of graphene after transfer to Si/SiO₂ reveal nanoripple arrays which are closely correlated with the Cu terraces. (d) Illustration of nanoripple formation, structure, and periodicity. (e) High-resolution scan with ultrasharp tips shows that the nanoripple consists of multiple peaks of 10–20 nm width.

step edges. The terrace structure is typically a few hundred nanometers in width, separated by step edges of ~ 100 nm in width. These parameters agree very well with the dimensions of NRAs. The patterning of Au alignment mark arrays on Cu right after graphene growth allows the direct correlation of the local Cu step edge pattern, density, and orientation with the surface morphology of graphene after it is transferred to a substrate. This comparison of graphene transferred from different Cu grains clearly demonstrates that NRAs originate from Cu step edges and, thus, rules out any other factors during the transfer and fabrication process (see Supporting Information). Previous studies^{6,7} proposed that the wrinkle formation (*i.e.*, out-of-plane mechanical deformations in graphene sheets on Cu) is sufficient to release strain arising from the difference in thermal expansion coefficients between graphene and Cu. The observation of high-density NRAs suggests that strain is, in fact, mainly released by high-density Cu step edges. Below we will show that at RT these NRAs ultimately also set a lower bound on the sheet resistance, R_{\square} , and an upper bound for the charge mobility, μ , even if all other extrinsic scatterings are eliminated.

We now focus on T -dependent electrical transport measurements. In micrometer size devices, the QHE is well-developed for both SLG and BLG, as shown in Figure 3a,b, respectively. From an application point of view, the zero field measurements of σ versus n are more relevant. They show a pronounced sublinear behavior, not only in CVD SLG but also in CVD BLG devices. The sublinearity is strongest at RT and diminishes gradually with decreasing temperature, as shown in Figure 3c,d, respectively. This is

best studied by plotting the T -dependent part of the resistivity instead and represents the key finding of our experiments. Our data reveal a superlinear T -dependent resistivity for $T > 50$ K. Remarkably, such a metallic behavior is observed in both SLG and BLG (Figure 3e). Previous studies on supported exfoliated samples only reported such a T -dependent resistivity in SLG, while BLG samples did not show any T dependence away from the charge neutrality point (CNP).²⁴ Such behavior for BLG is expected only for suspended samples, where the T -dependent contribution to ρ (n, T) scales as T^2/n and is generally associated with electron-flexural phonon (FP) scattering.²⁵ Indeed, the high-density NRAs effectively decouple up to 20% of CVD graphene sheets from the substrate, activating low-energy FP excitations in both SLG and BLG even when the samples are overall supported.

For CVD BLG, this clearly demonstrates that at RT NRAs will limit both R_{\square} and μ due to FP scattering. However, the CVD SLG case is more ambiguous. Its resistivity has additional T -dependent contributions due to scattering from remote interfacial phonons (RIP) of the SiO₂ substrate^{26,27} and possibly high-energy FPs arising from quenched 10 nm wide nanoripples.^{28,29} On SiO₂ substrates, both the FP and RIP scattering mechanisms lead to a very similar T - and n -dependent behavior over 50–350 K and $\sim 10^{12}/\text{cm}^2$ ranges (Figure 3e,f).²⁷

To explicitly measure the influence of NRAs on CVD SLG's resistivity, we have fabricated GFETs where the orientation of the electrodes is such that the current is either perpendicular (\perp) or parallel (\parallel) to the NRAs (Figure 4a,b). In total, four sets of devices have been characterized. Here we discuss representative data for

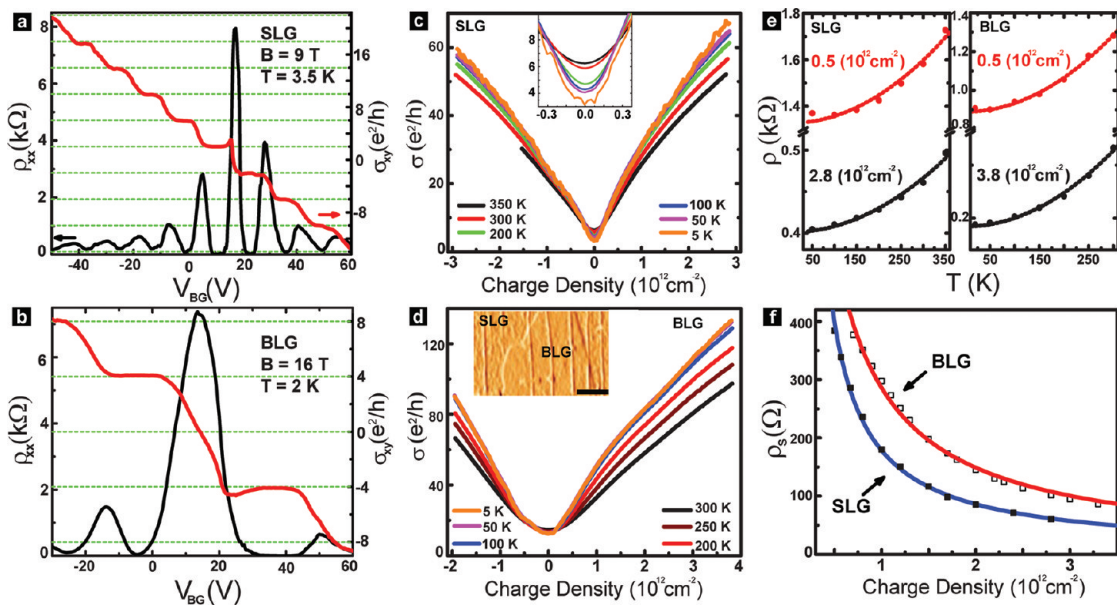


Figure 3. (a,b) QHE of CVD SLG and BLG graphene on Si/SiO₂ substrate, respectively. SLG shows the anomalous quantization plateaus of $\pm 4e^2/h(N + 1/2)$, while BLG has the typical $\pm 4Ne^2/h$ quantization signatures. (c) T -dependent sublinear behavior of a SLG. Inset: Insulating behavior with $n < 5 \times 10^{11}/\text{cm}^2$. (d) T -dependent sublinear behavior of a BLG. Inset: AFM image of a flower-shaped CVD BLG; quasi-periodic NRAs are clearly seen in both SLG and BLG; the scale bar is $1 \mu\text{m}$. (e) $\rho(T)$ for SLG at $n = 0.5 \times 10^{12}/\text{cm}^2$ and $n = 2.8 \times 10^{12}/\text{cm}^2$ and for BLG at $n = 0.5 \times 10^{12}/\text{cm}^2$ and $n = 3.8 \times 10^{12}/\text{cm}^2$. Dashed lines correspond to a two-parameter fit to the data using $\rho = \rho_0 + 0.1T + \gamma T^2/ne$ and serve as guide to the eyes. (f) RT superlinear contribution ρ_s to the total resistivity ρ as a function of charge density n for CVD SLG FET (black squares) and CVD BLG FET (white squares). The solid red and blue curves correspond to fits of the form $\rho_s = a/n$, where ρ_s arises from both FPs and RIPs. We used $a = 1.57 \times 10^{18}$ and $2.87 \times 10^{18} \Omega/\text{m}^2$ for SLG and BLG, respectively.

two sets (namely, S1 and S2). We analyzed the corresponding transport data by assuming a resistivity ρ of the form

$$\rho(n,T) = \rho_0(n) + \alpha T + \rho_s(n,T) \quad (1)$$

where $\rho_0(n)$ is the T -independent residual resistivity, αT is the acoustic phonon (AP)-induced resistivity ($\alpha = 0.1 \Omega/\text{K}$),²⁷ and $\rho_s(n,T)$ is the superlinear part of the resistivity. In Figure 4c,e, we directly compare $\rho_s(n,T)$ for the \perp and \parallel devices by computing the increase in resistivity between 100 K and T at fixed density n , namely, $\Delta\rho_{\perp}(n,T) = \rho_{\perp}(n,T) - \rho_{\perp}(n,100\text{ K}) - \alpha(T - 100\text{ K}) = \rho_{s\perp}(n,T) - \rho_{s\perp}(n,100\text{ K})$ and $\Delta\rho_{\parallel}(n,T) = \rho_{\parallel}(n,T) - \rho_{\parallel}(n,100\text{ K}) - \alpha(T - 100\text{ K}) = \rho_{s\parallel}(n,T) - \rho_{s\parallel}(n,100\text{ K})$. Strikingly, in both samples, $\Delta\rho_{\perp}$ remains always significantly greater than $\Delta\rho_{\parallel}$. In other words, the RT CVD graphene resistivity is anisotropic. This is in sharp contrast with the isotropic resistivity of exfoliated samples and clearly shows that the phonon scattering rate is higher in the devices with the \perp configuration. Since FPs are the only phonons which are activated upon suspension, this demonstrates that NRAs contribute also in CVD SLG importantly to the T dependence of ρ .

Assuming a simple resistor-in-series and resistor-in-parallel model (see Supporting Information), we estimate the impact of NRAs on key figures of merit such as μ and R_{\square} (Figure 4d). Note that in our model $\rho_s(n,T)$ arises from both electron-FP scattering (in the nanoripples) and electron-RIP scattering events

(between the nanoripples) independent of the NRA orientation. With this, we write $\rho_{s\perp} = f\rho_{FP} + (1 - f)\rho_{RIP}$ and $\rho_{s\parallel} = (f/\rho_{FP} + (1 - f)/\rho_{RIP})^{-1}$, where f is the ratio of the typical ripple width w and the mean inter-ripple spacing a . Besides, we assume ρ_{FP} is of the form $\gamma T^2/ne$,^{29–31} and ρ_{RIP} can be written as $(A/n)(g_1/\exp(E_1/(k_B T)) - 1) + g_2/\exp(E_2/(k_B T)) - 1$, where $g_1 = 3.2 \text{ meV}$ and $g_2 = 8.7 \text{ meV}$ are the respective coupling strengths of the SiO₂ RIP modes of energies $E_1 = 63 \text{ meV}$ and $E_2 = 149 \text{ meV}$.^{26,27} We can now estimate the two free parameters A and γ setting the magnitude of ρ_{FP} and ρ_{RIP} by fitting the curves of Figure 4c,e (see Supporting Information). This leads to $A \sim 3 \times 10^{17} \text{ k}\Omega/(\text{eV} \cdot \text{cm}^2)$, in reasonable agreement with refs 26 and 27, and $\gamma \sim 6 \times 10^{-6} \text{ V} \cdot \text{s}/(\text{mK})^2$. Interestingly, these extracted values of γ match well the experimental γ values recently obtained for fully suspended graphene samples.³⁰ With this, it is now possible to predict FP-induced limits on CVD SLG's μ and R_{\square} . Figure 4d shows the calculated RT mobility as a function of the helium- T mobility μ_0 for CVD graphene with $f = 20\%$ both in \perp and \parallel orientations. As μ_0 is unaffected by phonons, this is a convenient variable to gauge the influence of FPs.³² Including AP scattering NRAs limits the RT mobility to $\sim 40\,000 \text{ cm}^2/(\text{V} \cdot \text{s})$ in \perp orientation and $\sim 80\,000 \text{ cm}^2/(\text{V} \cdot \text{s})$ in \parallel orientation, independent of the choice of substrate. In contrast, RT mobilities greater than $100\,000 \text{ cm}^2/(\text{V} \cdot \text{s})$ have already been achieved for exfoliated graphene encapsulated in h-BN.³³

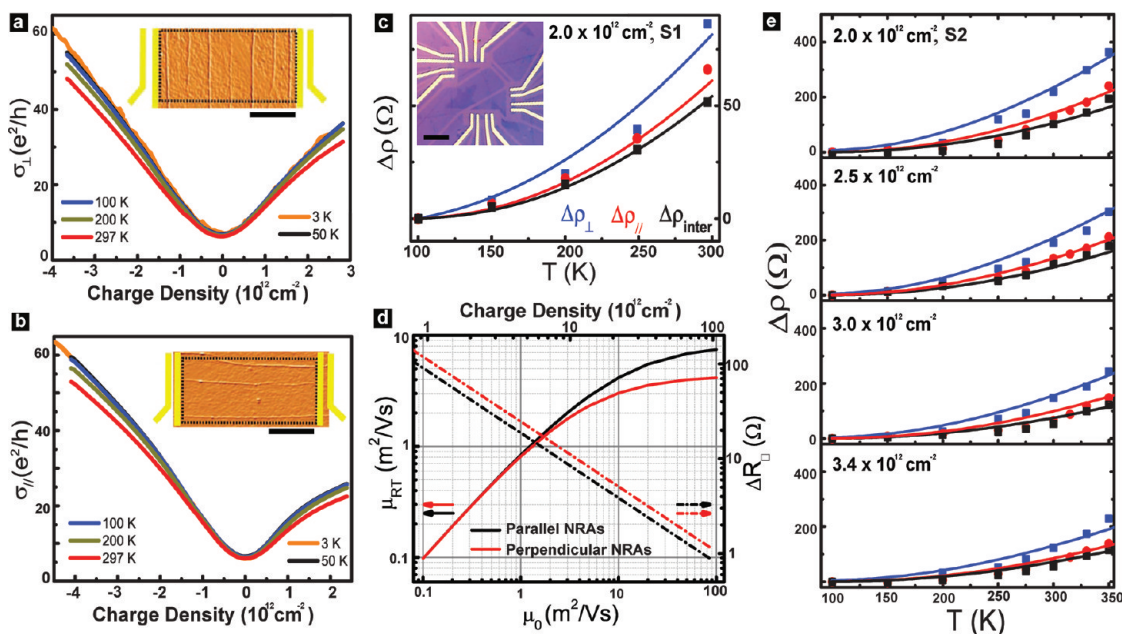


Figure 4. (a,b) T -dependent sublinear conductivity for both \perp and \parallel NRA configurations. Inset: AFM image of graphene channel with clear \perp and \parallel NRA orientations. The scale bar is $1 \mu\text{m}$. (c) Anisotropic resistivity results obtained with sample set S1 at $n = 2.0 \times 10^{12} \text{ cm}^{-2}$ (for data obtained at higher carrier density, see Supporting Information); the blue and red data points correspond to the \perp and \parallel NRA configurations, respectively. They are fitted with $\rho_{S\perp}(n,T) - \rho_{S\perp}(n,100 \text{ K})$ (solid blue) and $\rho_{S\parallel}(n,T) - \rho_{S\parallel}(n,100 \text{ K})$ (solid red). The black points correspond to $\Delta\rho_{\text{inter}}$ and are extracted from $\Delta\rho_{\perp}$ and $\Delta\rho_{\parallel}$ following the method described in the Supporting Information; $\Delta\rho_{\text{inter}}$ is fitted with $\rho_{\text{RIP}}(A,n,T) - \rho_{\text{RIP}}(A,n,100 \text{ K})$ with $A \sim 3 \times 10^{17} \text{ k}\Omega/\text{eV} \cdot \text{cm}^2$ (black solid curve). The inset shows the optical image of the device set. The scale bar is $10 \mu\text{m}$. (d) Estimate of the NRA impact on CVD SLG R_{\parallel} and μ at $n = 2 \times 10^{12} \text{ cm}^{-2}$. The solid red and black curves represent the RT mobility μ against liquid helium T mobility μ_0 for CVD SLG in both \perp (solid red) and \parallel (solid black) NRA configurations, assuming electron-RIP scattering is suppressed. The dashed dotted curves represent the FP-induced increase in R_{\parallel} in \perp (red) and \parallel (black) orientations. (e) Value of $\Delta\rho(T)$ obtained from a second set of devices S2 for different charge densities ranging from $2.0 \times 10^{12} \text{ cm}^{-2}$ to $3.4 \times 10^{12} \text{ cm}^{-2}$. The data points and fitting curves have the same definitions as described in (c).

CONCLUSIONS

For large-scale transparent electrodes and display applications at RT, R_{\square} is a more relevant number. Here, electron-FP scattering introduced by NRAs increases R_{\square} unacceptably, given the industry requirement of $R_{\square} \ll 100 \Omega$. At a technologically relevant carrier density of $1 \times 10^{12} \text{ cm}^{-2}$, the FP-induced increase in sheet resistance ΔR_{\square} alone is approximately 80Ω independent of the AP and RIP scattering induced contributions to the sheet resistance R_{\square} (Figure 4d). Various approaches may be employed to overcome this issue. One may either try to reduce the effect of NRAs by inducing high charge carrier densities ($\Delta R_{\square} \sim f_T T^2 / ne \sim 2 \Omega$ at $n = 5 \times 10^{13} \text{ cm}^{-2}$) and/or straining engineering,²⁵ or eliminating the NRAs altogether by transferring graphene under strain or using wet transfer processes which do not require any polymer coating. The rippling in CVD graphene can most likely never be fully avoided, but engineering Cu substrates

properly may significantly reduce their presence (see Supporting Information).

In summary, we show that the current growth and transfer methods of CVD graphene leads to quasi-periodic nanoripple arrays in graphene. Such high-density NRAs partially suspend graphene, giving rise to flexural phonon scattering. This not only causes anisotropy in charge transport but also sets limits on both the sheet resistance and the charge mobility even in the absence of grain boundaries. At room temperature, NRAs are likely to play a limiting role also for the mobility of ultraclean samples, in particular, when the graphene sheets are transferred onto ultraflat BN substrates.^{11,12} On the other hand, the controlled rippling of graphene (Supporting Information) may be useful for graphene-based sensor applications as the ripples are more prone to adsorptions than flat graphene.³⁴ Controlled rippling may also be instrumental for spin-based device applications requiring surface modifications.³⁵

METHODS

CVD Graphene Synthesis. The synthesis and transfer of large-scale CVD graphene are the same as in ref 7. Electron back-scattering diffraction reveals that the annealed Cu(001) substrates have single-crystal patches of Cu(111) and Cu(101),

indicating local surface melting and recrystallization during growth (see Supporting Information). The grain size of our CVD graphene is $\sim 50\text{--}100 \mu\text{m}$, as determined by scanning electron microscopy (SEM) of submonolayer graphene on Cu foil (Figure 1a). We can synthesize CVD graphene with a high

BLG coverage up to 40% (Figure 1b) or SLG-dominant samples (>95%).¹⁸ Raman spectra (Figure 1c) show insignificant defect peaks demonstrating the high quality of both SLG and A–B stacked BLG. Except for areas with optically visible wrinkles, Raman imaging with micrometer resolution also shows that on this scale strain is negligible (Figure 1c and Supporting Information). Furthermore, scanning Kelvin probe microscopy is used to confirm energy favorable A–B stacking structure³⁶ in CVD BLG (see Supporting Information).

AFM Measurements. Both high-resolution contact mode and tapping mode AFM technique have been utilized to characterize graphene morphology on top of copper and on top of the Si/SiO₂ substrate. For contact mode AFM, ultrasharp tips with radii as small as 10 nm were used, limiting the error to ~10% error when measuring the 100 nm nanorippled area in Figure 2 and SFig 4. However, the contact mode AFM tips are more vulnerable to surface contaminations. Thus, for large-scale characterization, tapping mode AFM was used.

Raman Spectroscopy. Raman spectroscopy/imaging was carried out with a WITEC CRM200 Raman system with 532 nm (2.33 eV) excitation and laser power at sample below 0.1 mW to avoid laser-induced heating. A 100× objective lens with a NA = 0.95 was used in the Raman experiments. To obtain the Raman images (see Supporting Information), a piezo stage was used to move the sample with step size of 200 nm, and Raman spectrum was recorded at every point. The stage movement and data acquisition were controlled using ScanCtrl Spectroscopy Plus software from WITec GmbH, Germany. Data analysis was done using WITec Project software.

Graphene FET Device Fabrication. Graphene field-effect transistor (GFET) Hall bars and four-terminal devices ranging in size from 1.2×0.8 to $100 \times 10 \mu\text{m}^2$ were patterned by e-beam lithography (EBL) for metal contacts (5 nm Cr/30 nm Au) and O₂ plasma etching. Very large-scale GFETs of $1.2 \times 1.2 \text{ mm}^2$ were etched into van der Pauw geometry by EBL followed by metal contact evaporation using shadow masks. To precisely define four contacts either perpendicular or parallel with the NRAs, Au alignment mask arrays were prepatterned using standard EBL processes followed by systematic noncontact mode atomic force microscopy (AFM) scanning. The devices were finally thermally annealed at 400 K in high vacuum level (10^{-5} mbar) for 2 h to clean the graphene working channel.

Transport Measurements. Electrical transport measurements were done in vacuum in a four-contact configuration using a lock-in amplifier with an excitation current of 100 nA. *T*-dependent measurements were done from 350 to 2 K in variable temperature insert (VTI) using standard four-contact lock-in techniques. In total, eight SLG devices and three BLG devices have been measured. Here we discuss five (two) representative SLG (BLG) devices in more detail.

Conflict of Interest: The authors declare no competing financial interest.

Acknowledgment: We thank Chun-Xiao Cong and Ting Yu for Raman characterization of Cu-CVD graphene, Xiang-Ming Zhao, Jayakumar Balasubramanian, Kai-Wen Zhang, Xiang-Fan Xu, Chee-Tat Toh for assisting in device fabrications, and Manu Jaiswal for useful discussions. This work is supported by the Singapore National Research Foundation Grant NRF-RF2008-07, NUS/SMF grant, U.S. Office of Naval Research (ONR and ONR Global), and A*STAR SERC TSRP-Integrated Nanophoto-Bio Interface (R-144-000-275-305), NUS NanoCore, and by Basic Science Research Program (2011K000615, 2011-0017587, 2011-0006268) and Global Research Lab (GRL) Program (2011-0017587) through the National Research Foundation of Korea (NRF) funded by the Ministry of Education, Science, and Technology.

Supporting Information Available: (1) Ultralarge copper grain size by pregrowth annealing, (2) SKPM of CVD-grown graphene on Cu, (3) correlation of structure of Cu and CVD graphene after wet transfer, (4) CVD graphene transferred on Si/SiO₂ substrate without any other support, (5) how to avoid nanoripple arrays, (6) *T*-dependent sublinear conductivity in CVD BLG FETs, (7) Raman spectroscopy 2-D mapping of CVD SLG device, (8) modeling of the anisotropic resistivity, (9) method used to extract *A* and γ for ρ_{RIP} and ρ_{FP} , (10) anisotropic resistivity as a

function of charge density for sample set S1. This material is available free of charge via the Internet at <http://pubs.acs.org>.

REFERENCES AND NOTES

- Geim, A. K. Graphene: Status and Prospects. *Science* **2009**, *324*, 1530–1534.
- Novoselov, K. S.; Geim, A. K.; Morozov, S. V.; Jiang, D.; Katsnelson, M. I.; Grigorieva, I. V.; Dubonos, S. V.; Firsov, A. A. Two-Dimensional Gas of Massless Dirac Fermions in Graphene. *Nature* **2005**, *438*, 197–200.
- Castro Neto, A. H.; Guinea, F.; Peres, N. M. R.; Novoselov, K. S.; Geim, A. K. The Electronic Properties of Graphene. *Rev. Mod. Phys.* **2009**, *81*, 109–162.
- Bonaccorso, F.; Sun, Z.; Hasan, T.; Ferrari, A. C. Graphene Photonics and Optoelectronics. *Nat. Photonics* **2010**, *4*, 611–622.
- Zheng, Y.; Ni, G. X.; Toh, C. T.; Zeng, M. G.; Chen, S. T.; Yao, K.; Özyilmaz, B. Gate-Controlled Non-volatile Graphene-Ferroelectric Memory. *Appl. Phys. Lett.* **2009**, *94*, 163505.
- Li, X.; Cai, W.; An, J.; Kim, S.; Nah, J.; Yang, D.; Piner, R.; Velamakanni, A.; Jung, I.; Tutuc, E.; et al. Large-Area Synthesis of High-Quality and Uniform Graphene Flms on Copper Foils. *Science* **2009**, *324*, 1312–1314.
- Bae, S.; Kim, H.; Lee, Y.; Xu, X.; Park, J. S.; Zheng, Y.; Balakrishnan, J.; Lei, T.; Kim, H. R.; Song, Y.; et al. Roll-to-Roll Production of 30-Inch Graphene Fims for Transparent Electrodes. *Nat. Nanotechnol.* **2010**, *5*, 574–578.
- Lee, S.; Lee, K.; Zhong, Z. H. Wafer Scale Homogeneous Bilayer Graphene Films by Chemical Vapor Deposition. *Nano Lett.* **2010**, *10*, 4702–4707.
- Zheng, Y.; Ni, G. X.; Toh, C. T.; Tan, C. Y.; Yao, K.; Özyilmaz, B. Graphene Field Effect Transistors with Ferroelectric Gating. *Phys. Rev. Lett.* **2010**, *105*, 166602.
- Zheng, Y.; Ni, G. X.; Bae, S.; Cong, C. X.; Kahya, O.; Toh, C. T.; Kim, H. R.; Im, D.; Yu, T.; Ahn, J. H.; et al. Wafer-Scale Graphene/Ferroelectric Hybrid Devices for Low-Voltage Electronics. *Europhys. Lett.* **2011**, *93*, 17002.
- Dean, C. R.; Young, A. F.; Meric, I.; Lee, C.; Wang, L.; Sorgenfrei, S.; Watanabe, K.; Taniguchi, T.; Kim, P.; Shepard, K. L.; et al. Boron Nitride Substrates for High Quality Graphene Electronics. *Nat. Nanotechnol.* **2010**, *5*, 722–726.
- Gannett, W.; Regan, W.; Watanabe, K.; Taniguchi, T.; Crommie, M. F.; Zettl, A. Boron Nitride Substrates for High Mobility Chemical Vapor Deposited Graphene. *Appl. Phys. Lett.* **2011**, *98*, 242105.
- Pereira, V. M.; Castro Neto, A. H. Strain Engineering of Graphene's Electronic Structure. *Phys. Rev. Lett.* **2009**, *103*, 046801.
- Low, T.; Guinea, F.; Katsnelson, M. I. Gaps Tunable by Gates in Strained Graphene. *Phys. Rev. B* **2011**, *83*, 195436.
- Reina, A.; Jia, X. T.; Ho, J.; Nezich, D.; Son, H.; Bulovic, V.; Dresselhaus, M. S.; Kong, J. Large Area, Few-Layer Graphene Films on Arbitrary Substrates by Chemical Vapor Deposition. *Nano Lett.* **2009**, *9*, 30–35.
- Kim, K. S.; Zhao, Y.; Jang, H.; Lee, S. Y.; Kim, J. M.; Kim, K. S.; Ahn, J. H.; Kim, P.; Choi, J. Y.; Hong, B. H.; et al. Large-Scale Pattern Growth of Graphene Films for Stretchable Transparent Electrodes. *Nature* **2009**, *457*, 706–710.
- Rasool, H. I.; Song, E. B.; Allen, M. J.; Wassei, J. K.; Kaner, R. B.; Wang, K. L.; Weiller, B. H.; Gimzewski, J. K. Continuity of Graphene on Polycrystalline Copper. *Nano Lett.* **2011**, *11*, 251–256.
- Li, X. S.; Magnuson, C. W.; Venugopal, A.; Tromp, R. M.; Hannon, J. B.; Vogel, E. M.; Colombo, L.; Ruoff, R. S. Large-Area Graphene Single Crystals Grown by Low-Pressure Chemical Vapor Deposition of Methane on Copper. *J. Am. Chem. Soc.* **2011**, *133*, 2816–2819.
- Li, X. S.; Magnuson, C. W.; Venugopal, A.; An, J.; Suk, J. W.; Han, B.; Borysiak, M.; Cai, W.; Velamakanni, A.; Zhu, Y.; et al. Graphene Films with Large Domain Size by a Two-Step Chemical Vapor Deposition Process. *Nano Lett.* **2010**, *10*, 4328–4334.
- Wofford, J. M.; Nie, S.; McCarty, K. F.; Bartelt, N. C.; Dubon, O. D. Graphene Islands on Cu Foils: The Interplay between

- Shape, Orientation, and Defects. *Nano Lett.* **2010**, *10*, 4890–4896.
21. Zhang, Y. F.; Teng, G.; Gao, Y. B.; Xie, S. B.; Ji, Q. Q.; Yan, K.; Peng, H. L.; Liu, Z. F. Defect-like Structures of Graphene on Copper Foils for Strain Relief Investigated by High Resolution Scanning Tunneling Microscopy. *ACS Nano* **2011**, *5*, 4014–4022.
22. Yu, Q. K.; Jauregui, L. A.; Wu, W.; Colby, R.; Tian, J.; Su, Z.; Cao, H.; Liu, Z.; Pandey, D.; Wei, D.; et al. Control and Characterization of Individual Grains and Grain Boundaries in Graphene Grown by Chemical Vapour Deposition. *Nat. Mater.* **2011**, *10*, 443–449.
23. Lahiri, J.; Lin, Y.; Bozkurt, P.; Oleynik, I. I.; Batzill, M. An Extended Defect in Graphene as a Metallic Wire. *Nat. Nanotechnol.* **2010**, *5*, 326–329.
24. Morozov, S. V.; Novoselov, K. S.; Katsnelson, M. I.; Schedin, F.; Elias, D. C.; Jaschczak, J. A.; Geim, A. K. Giant Intrinsic Carrier Mobilities in Graphene and Its Bilayer. *Phys. Rev. Lett.* **2008**, *100*, 016601.
25. Ochoa, H.; Castro, E. V.; Katsnelson, M. I.; Guinea, F. Temperature Dependent Resistivity in Bilayer Graphene Due to Flexural Phonons. *Phys. Rev. B* **2011**, *83*, 235416.
26. Zou, K.; Hong, X.; Keefer, D.; Zhu, J. Deposition of High-Quality HfO_2 on Graphene and the Effect of Remote Oxide Phonon Scattering. *Phys. Rev. Lett.* **2010**, *105*, 126601.
27. Chen, J. H.; Jang, C.; Xiao, S. D.; Ishigami, M.; Fuhrer, M. S. Intrinsic and Extrinsic Performance Limits of Graphene Devices on SiO_2 . *Nat. Nanotechnol.* **2008**, *3*, 206–209.
28. Kusminskiy, V. S.; Campbell, D. K.; Castro Neto, A. H.; Guinea, F. Pinning of a Two-Dimensional Membrane on Top of a Patterned Substrate: The Case of Graphene. *Phys. Rev. B* **2011**, *83*, 165405.
29. Katsnelson, M. I.; Geim, A. K. Electron Scattering on Microscopic Corrugations in Graphene. *Philos. Trans. R. Soc., A* **2008**, *366*, 195–204.
30. Castro, E. V.; Ochoa, H.; Katsnelson, M. I.; Gorbachev, R. V.; Elias, D. C.; Novoselov, K. S.; Geim, A. K.; Guinea, F. Limits on Charge Carrier Mobility in Suspended Graphene Due to Flexural Phonons. *Phys. Rev. Lett.* **2010**, *105*, 266601.
31. Mariani, E.; Oppen, F. V. Temperature-Dependent Resistivity of Suspended Graphene. *Phys. Rev. B* **2010**, *82*, 195403.
32. In our estimate, we assumed no electron-RIP scattering for CVD graphene at RT since it can, in principle, be suppressed by choosing a proper substrate.
33. Mayorov, A. S.; Gorbachev, R. V.; Morozov, S. V.; Britnell, L.; Jalil, R.; Ponomarenko, L. A.; Blake, P.; Novoselov, K. S.; Watanabe, K.; Taniguchi, T.; et al. Micrometer-Scale Ballistic Transport in Encapsulated Graphene at Room Temperature. *Nano Lett.* **2011**, *11*, 2396–2399.
34. Elias, D. C.; Nair, R. R.; Mohiuddin, T. M. G.; Morozov, S. V.; Blake, P.; Halsall, M. P.; Ferrari, A. C.; Boukhvalov, D. W.; Katsnelson, M. I.; Geim, A. K.; et al. Control of Graphene's Properties by Reversible Hydrogenation: Evidence for Graphane. *Science* **2009**, *323*, 610–613.
35. Avsar, A.; Yang, T. Y.; Bae, S.; Balakrishnan, J.; Volmer, F.; Jaiswal, M.; Zheng, Y.; Ali, S. R.; Guntherodt, G.; Hong, B. H.; et al. Toward Wafer Scale Fabrication of Graphene Based Spin Valve Devices. *Nano Lett.* **2011**, *11*, 2363–2368.
36. Yu, Y. J.; Zhao, Y.; Ryu, S.; Brus, L. E.; Kim, K.; Kim, P. Tuning the Graphene Work Function by Electric Field Effect. *Nano Lett.* **2009**, *9*, 3430–3434.